# Mapping nanomechanical properties of freshly grown, native, interlamellar organic sheets on flat pearl nacre ☆

Malte Launspach [a], Katharina I. Gries [c], Fabian Heinemann [d], Anja Hübner [a], Monika Fritz [a], Manfred Radmacher [b],*

[a] Pure and Applied Biomineralisation Group, Institute of Biophysics, University of Bremen, Bremen, Germany
[b] Institute of Biophysics, University of Bremen, Bremen, Germany
[c] Materials Science Center and Department of Physics, Philipps University of Marburg, Marburg, Germany
[d] Roche Diagnostics, Penzberg, Germany

## ARTICLE INFO

## ABSTRACT

We imaged surfaces of freshly grown flat pearl nacre (*Haliotis tuberculata*) in different stages of growth in seawater using an atomic force microscope (AFM). Characteristic mineral phases of nacre, such as aragonitic stacks of coins, as well as the associated organic sheets, could be detected. Apart from imaging, the acquisition of force volumes on freshly grown organic surface areas on flat pearl nacre was conducted with the AFM. The evaluation of the force volumes with the Hertz–Sneddon model resulted in Young's moduli in the MPa range. The presented values are considerably smaller than values previously determined from macroscopic tensile tests. This might reflect the anisotropy of the organic nacre layers.

© 2014 Acta Materialia Inc. Published by Elsevier Ltd. All rights reserved.

## 1. Introduction

Nacre is a natural composite with a high content of a mineral phase (~98 wt.%) and a small portion of organic material (~2 wt.%). This small portion of organic material is responsible for the distinct structure of nacre. As can be seen from Fig. 1, mineral platelets (aragonite) grow between organic sheets (interlamellar matrix). This distinct structure – mineral platelets of a defined geometry and organic sheets between them – is responsible for the interesting mechanical properties of nacre. This biocomposite is a tough material although its mineral components do not have this property. Often, common minerals show stiff and brittle behaviour. Less is known about the properties of the thin organic sheets (see e.g. Ref. [1] for a recent study on the interfaces within nacre). The mechanical testing of the whole composite material and the mineral parts has been the subject of many studies (for recent reviews of nacre and its properties, see e.g. Refs. [2–4]).

Recently, two approaches have been used to access the mechanical properties of the organic sheets of demineralized nacre pieces of *Haliotis* sp. in wet conditions. Bezares et al. [5] probed

macroscopic specimens of demineralized nacre pieces from *Haliotis rufescens* in different conditions in a macroscopic tensile test system. They described the organic sheets in terms of a standard linear solid model. Dastjerdi et al. [1] probed demineralized organic sheets from red abalone, pearl oyster and top shell with a similar approach. They reported a modulus of 136 MPa for the organic matrix from red abalone.

Our group [6] probed the demineralized organic sheets of nacre of *Haliotis laevigata* in aqueous solution with the atomic force microscopy (AFM) force mapping technique and derived values for the Young's modulus below 1 MPa in the fully hydrated state.

Flat pearls [7] (cf. Fig. 1E and F) can be used to prepare freshly grown, native, hydrated interlamellar organic sheets from growth front nacre (cf. Fig. 1A) as well as other organic phases close to their natural state. The animal deposits shell material on glass slides in a defined sequence [8], when inserted between mantle epithelium and shell as a support (cf. Fig. 1D–F). In a polymer cushion crystals are grown.

In contrast to the flat pearls of *H. rufescens* (e.g. [8–10]) the different layers of flat pearls from *H. tuberculata* seem not to be characterized yet. However, Fleury et al. [11] investigated repair processes in the shell of *H. tuberculata*. They imaged the sequence of different layers during the shell formation process. Fritz et al. [7], Zaremba et al. [8] and Fleury et al. [11] could show in *H. rufescens* and *H. tuberculata*, respectively, that the deposition of shell material on glass and the deposition during the repair
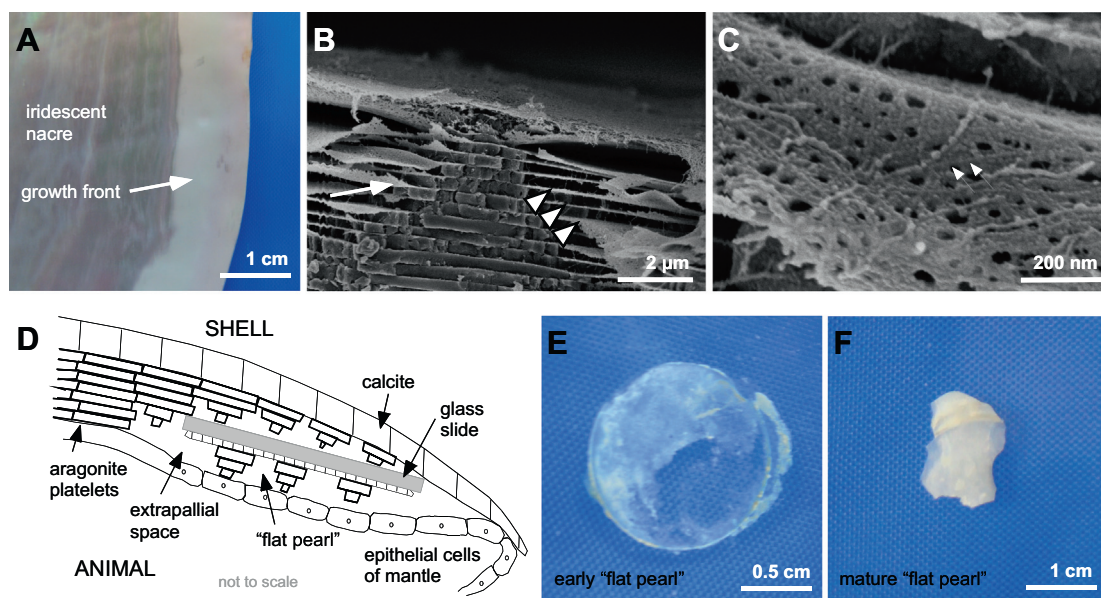
**Fig. 1.** Nacre of natural shell of *Haliotis laevigata* (A) and biogenic flat pearl of the seawater snail *Haliotis tuberculata* (B, C, E, F). (A) Photograph taken from the outermost part of nacre of a shell (*H. laevigata*). The growth front of the shell (white arrow) has a whitish appearance due to light scattering on the stacks of coins (see mineral part in (B)). Iridescent nacre is formed by thin confluent aragonite layers due to interference of visible light. (B) SEM image of stacks of coins (white arrow) of aragonite crystals horizontally intercalated by multilamellar organic sheets (white arrowheads) of protein decorated chitin filaments (white arrows in (C)). (C) SEM image of a network with holes/pores constructed by protein decorated chitin filaments (white arrows). (D) Sketch of a "flat pearl" inserted between mantle epithelium and the shell. The inserted glass slide is overgrown by shell material in a defined sequence. (E) Photograph of an "early flat pearl", which was inserted for less than 3 weeks. (F) Photograph of a "mature flat pearl", which was inserted for more than 5 weeks. The overgrowth with growth front nacre is clearly visible.

process are comparable to the deposition of shell material in the natural shell.

Therefore we assume in the following that the sequence and type of layers deposited during flat pearl growth are similar to the genus *Haliotis*. As a first step of flat pearl mineralization, islands of prismatic calcite (or in some cases spherulitic aragonite) expand until they cover the entire surface. If the crystals are prismatic calcite then this organic surface resembles the periostracum of the natural shell. A mixture of secreted proteins is necessary for an ongoing calcite growth. On a certain signal, which is not understood yet, the epithelial cells seem to switch to the secretion of a protein set, which then enables the growth of another calcium carbonate crystal polymorph: aragonite. Aragonite tablets start to grow in a preformed organic matrix (cf. Fig. 1C), where multilamellar sheets of organic material are deposited first. The tablets grow in so-called stacks of coins, where the first crystal is nucleated in an unknown way on one of these organic sheets in its crystallographic *c*-direction pointing perpendicular to the surface. The crystal grows until it reaches a height of ∼0.5 μm as a small stencil and later in the crystallographic *a*- and *b*-directions. Long before it reaches its final lateral dimensions, a new crystal starts to grow on top of it (Fig. 1B and D), passing the crystal orientation to the next layer [12] by a so-called mineral bridge. Horizontally between each crystal layer one multilamellar sheet of a protein embedded chitin network is located (Fig. 1B, white arrowheads, and Fig. 1C) [2,13].

In this study we measured the elastic properties of the native, hydrated organic matrix, which is freely accessible between the freshly grown aragonitic stacks of coins and other calcium carbonate mineral phases.

The advantage of the thus prepared samples is that organic sheets are of a defined age and may be used without any further preparatory means. They may be imaged and probed in aqueous solution (here: seawater) by AFM to investigate their mechanical properties.

We will show in the next paragraphs the topography of the sequentially deposited material from the first mineral layers to the first nucleation of aragonite tablets to a fully covered sample by stacks of coins, which resembles the growth front of a natural shell (Fig. 1A).

Furthermore, we will show the results of force–indentation measurements conducted with the AFM on three fully hydrated flat pearl samples in aqueous solution. The flat pearls can provide organic layers that can be probed with the AFM without further treatments like demineralization. The Hertz–Sneddon model is used to obtain information on the Young's modulus of the probed samples.

## 2. Materials and methods

### 2.1. Sample preparation

Cover glass discs with a diameter of 5 or 10 mm were inserted between the shell and the mantle epithelium of the snail *H. tuberculata*. The animals are kept in a seawater aquarium at 15–17 °C at our institute. The seawater snail *H. tuberculata* is abundant in the Mediterranean Sea and the East Atlantic Ocean, e.g. at the coast of France. The animals, which deposited nacre on an inserted glass slide, were raised at abalone farms in France and Germany (SCEA France Haliotis, Plougerneau, France and Sylter Algenfarm GmbH, List/Sylt, Germany) and specimens of different ages were purchased by us. They have lived for several years in a seawater tank with natural seawater collected from the North Sea (close to Helgoland) provided by the Alfred Wegener Institute, Bremerhaven (Germany).

After different periods of time (for different growth stages) the cover glasses were removed from the snails and prepared for imaging. From the removal until imaging the so-formed flat pearls were stored in filtered (Millex-GV, PVDF membrane, pore size 0.22 μm, Millipore Ireland Ltd) seawater (North Sea water, collected and kindly provided by the Alfred-Wegener-Institut für Polar- und Meeresforschung, Bremerhaven, Germany). The absence of plankton and bacteria, which could otherwise influence our measurements, was tested by light microscopy after filtering the water.
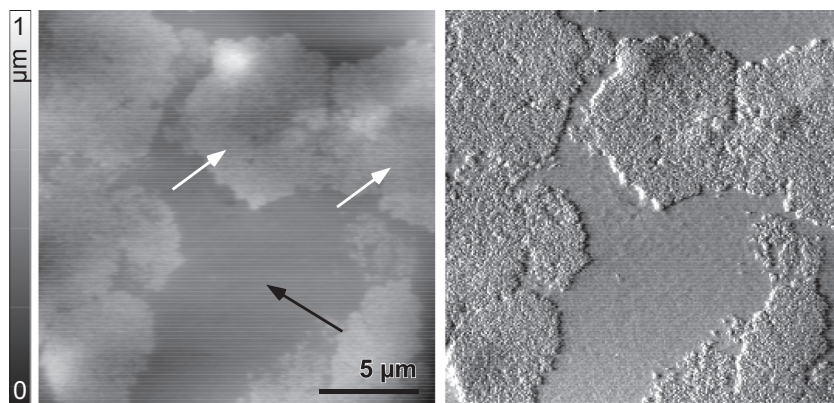
**Fig. 2.** AFM image (height image on the left and deflection image on the right) of an "early flat pearl" (cover glass was inserted for several weeks) with organic material resembling the periostracum (black arrow) and a mineral part, which is possibly calcite (white arrows).

For the measurements in the AFM either the overgrown cover glasses or fragments of the grown flat pearls were glued into a plastic Petri dish with an epoxy glue (Bindulin, Fürth, Germany), which needs 5 min to cure. During the curing process the flat pearl was kept hydrated in a droplet of filtered seawater. After hardening of the glue, seawater was added to the Petri dish so that the flat pearl was completely immersed in liquid. During the whole preparation and imaging process the flat pearl was never allowed to dry.

For scanning electron microscopy (SEM) the samples (shown in Fig. 1B and C) were prepared with the following procedure. Fragments of the growth front region of the shell of *H. tuberculata* (living animals obtained from Sylvain Huchette, France Haliotis, Plouguerneau, France) were fixed for 1 h in a solution consisting of 2.5% glutaraldehyde (Agar Aids, Cambridge, UK), 2% paraformaldehyde (Merck, Darmstadt, Germany), 0.1 M cacodylate buffer (pH 7.4, Fluka, Sigma–Aldrich GmbH, Steinheim, Germany) and 262 mg/15 ml seasalt (Tropic Marin, Dr. Biener GmbH, Wartenberg, Germany). Afterwards the shell fragments were washed with 0.1 M cacodylate buffer, prefixed and stained with 2% osmium tetroxide (Agar Aids, Cambridge, UK) and 0.8% potassium hexacynoferrate (Merck, Darmstadt, Germany) and again washed with 0.1 M cacodylate buffer two to three times for 5–10 min, respectively. The shell fragments were dehydrated in a graded isopropanol series until 100% isopropanol was reached. After substitution of isopropanol (Merck, Darmstadt, Germany) with carbon dioxide

the samples were critical point dried (BAL-TEC CPD030 Critical Point Dryer, Wetzlar, Germany). Before investigating the samples with SEM, they were rotary-shadowed with 3 nm platinum (Balzers AG, BAF 100, Balzers, Liechtenstein). The field emission SEM (Hitachi S-5200, Tokyo, Japan) was operated in secondary electron imaging mode at an acceleration voltage of 4 kV.

The flat pearl presented in Fig. 4A was produced by placing a silicon wafer between the shell and the mantle epithelium of *H. tuberculata* and removing it after 13 days. Directly after the removal the flat peal was rinsed with Milli-Q water (Millipore, Academic QGard2, Billerica, MA, USA) and dried with a stream of gaseous nitrogen. After coating the sample with gold in a vapour deposition system it was investigated in a field emission scanning electron microscope (FEI, Nova 200, Eindhoven, the Netherlands) which was operated in secondary electron imaging mode at an acceleration voltage of 5 kV.

### 2.2. AFM imaging and acquisition of force volumes

AFM investigations of the surface structure of the flat pearl were carried out with an MFP-3D-Bio AFM (Asylum Research, Santa Barbara, CA, USA) using contact mode. Height and error signal were monitored. During imaging, care was taken to use the lowest possible force.

A silicon nitride cantilever (Microlevers, MSCT-AUHW, Veeco, Santa Barbara, CA, USA) was used for imaging and force–indentation
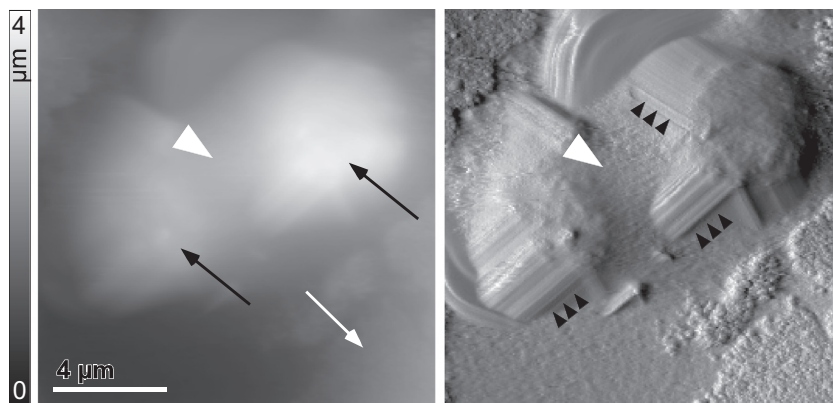


**Fig. 3.** AFM image of the same sample as in Fig. 2 with aragonite crystals (black arrows) starting to grow on the calcite islands (or spherulitic aragonite) (white arrow). The left image shows the height image and the right image the deflection image. Prominent features are parallel streaks at the edge of the stacks (black arrowheads on deflection image) from the side (flank) of the tip. It touches the crystal because of its high (~0.5 μm), steep edge, before the very end of the tip can reach the sample. At these regions no valuable data may be extracted.
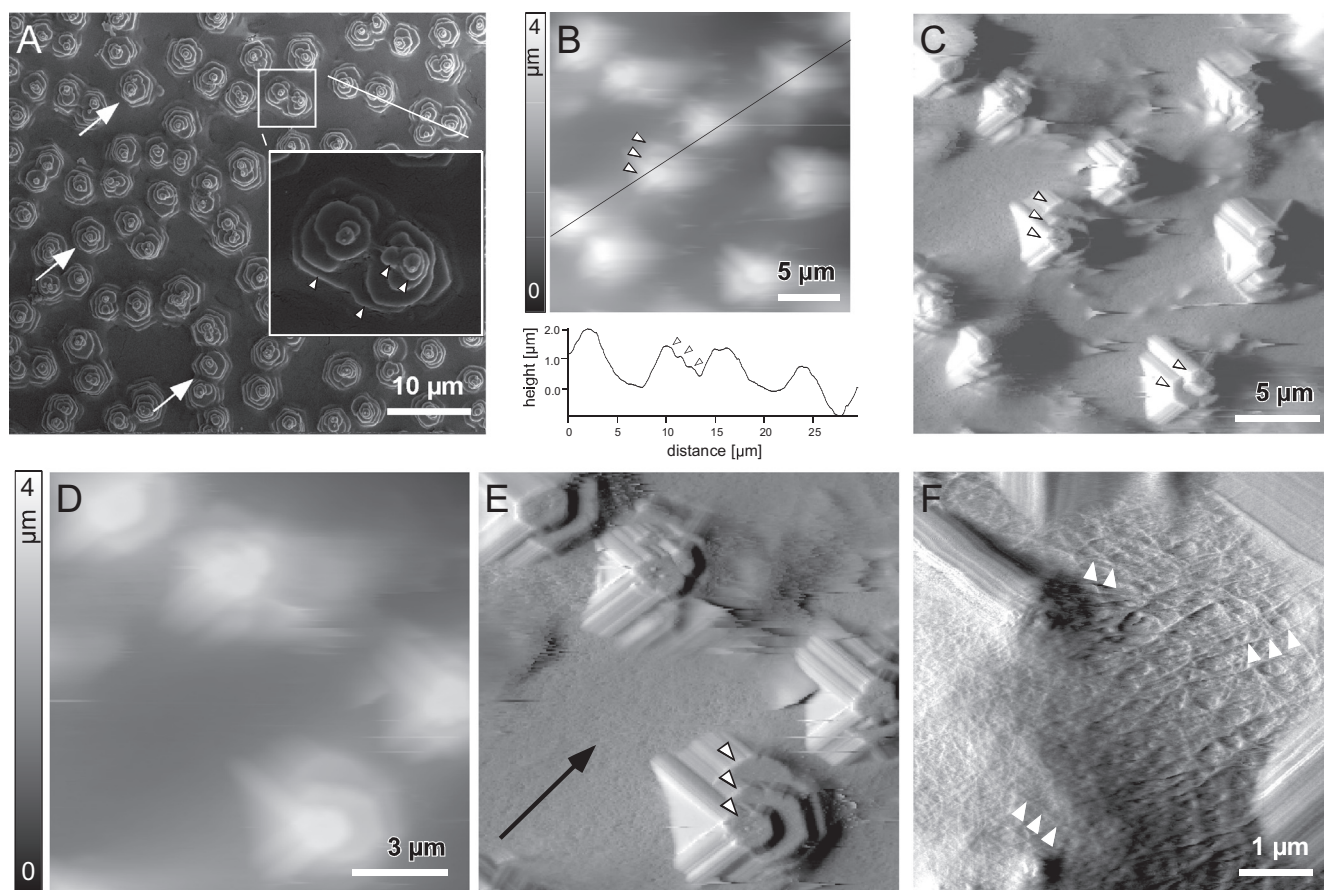
**Fig. 4.** SEM image and AFM images of several mature flat pearls (*Haliotis tuberculata*) of different ages. (A) SEM image with stacks (white arrows pointing on examples) with more than five tablets on top of each other. The inset shows the occasional growth of more than one tablet (arrowheads) on top of the underlying one. (B) AFM height image with profile along the line showing the height of the tablets (white arrowheads) being ∼0.5 μm. (C) AFM deflection (or error signal of (B)) with arrowheads on consecutive tablets in a stack. (D) Close-up view of image in (C) (height signal). (E) Corresponding deflection (error) signal. The surfaces of the single tablets (white arrowheads) are clearly visible. In between the stacks of coins the interlamellar matrix (black arrow) shows a network-like structure. (F) Close-up view (deflection) of the interlamellar matrix between the stacks of coins shown in Fig. 3. It is obvious that the matrix is located not only between the stacks, but also on top of the uppermost tablet (white arrowheads), which runs in the interspace of the tablets and also over the tablet itself.

measurements. According to the manufacturer's data the nominal spring constant of the cantilever used was 30 pN nm$^{-1}$ and the nominal resonance frequency in air was stated as 15 kHz. The tip shape was that of a square pyramid with a total height of ∼3 μm. The last 200 nm (beginning at the tip apex) were sharpened (by the manufacturer). The result of the sharpening was a nominal tip half opening angle of 18°.

Several chips with the AFM cantilevers were cleaned in an argon–oxygen plasma (TPS 216 EC, Binder Labortechnik, Hebertshausen, Germany) for 1 min and then stored in a box with gel coated bottom (Gel-Pak). We use plasma cleaning routinely and found that tip sharpness is not sacrificed, as determined by high-resolution imaging of calcite surfaces. We also have not observed any change in resonance frequency resulting from material loss or gain from the plasma treatment.

Prior to any AFM imaging and force mapping the resonance frequency of the cantilever's thermal driven motion in air was determined. The resonance frequencies of the used cantilevers in air were 15.6, 16.5 and 16.0 kHz, i.e. close to the specified nominal resonance frequency of 15 kHz. The spring constants determined with the thermal noise method (e.g. [14,15]), as implemented in the AFM by the manufacturer, were unreasonably high in two cases (between 50 and 55 pN nm$^{-1}$). Therefore we estimated the spring constants with the measured resonance frequency according to Eq. (6) in Ref. [16]. These estimates were 34, 40 and 37 pN nm$^{-1}$, close to the nominal spring constant of 30 pN nm$^{-1}$.

In the following we will refer to three samples. These three samples differ (at least) in the time period in which they remained between shell and animal. Sample 1 remained about 3–4 weeks in the extrapallial space, while samples 2 and 3 stayed 5–7 weeks between shell and animal. Not every glass slide, which is deposited between mantel epithelium and shell of a snail, stays in place to be overgrown. Thus on control of the slides in the animals we had to put in new slides, because the first or even the second one was removed by the animals. This is the reason why the samples we investigated have different ages.

Flat pearl sample 2 or fragments thereof were imaged at two different times in the AFM. After the first imaging the flat pearl (or fragments thereof) was (were) stored for 5 weeks in 0.22 μm filtered seawater containing 0.02% NaN$_3$ at 5–6 °C. Prior to the second imaging it was purged with seawater. The data shown here are from the second investigation.

Several samples were investigated by AFM force mapping. The goal was to record large area, high-resolution force maps, since we were expecting very inhomogenous samples. Thus we typically recorded 50 × 50 force curves over an area of 10 or 20 μm, resulting in a spacing of 0.4 or 0.2 μm. Maximum deflection was set to 200 nm, corresponding to a maximum loading force of 6 nN. The indentation, depending on sample stiffness, was on the order of 200 nm to 1 μm. This allowed us to check whether the elastic properties of the sample changed as a function of depth when analysing different parts of the force curves. Since the indentation will also

limit the lateral resolution achievable, it is not helpful to further decrease the spacing of force curves.

On flat pearl sample 1 three force maps were analyzed. The first force map consisted of 50 × 50 force curves on a 20.0 μm × 20.0 μm area. The force scan rate was 1 Hz (tip velocity 1.98 μm s$^{-1}$) and a relative deflection threshold of 200 nm was used. The second force map was recorded on a different spot with 20 × 20 force curves on a 5.8 μm × 5.8 μm area. The force scan rate, tip velocity and relative deflection threshold were the same as in the aforementioned case. The third force map was recorded on the same spot as the second map of sample 1 but with a higher relative deflection threshold of 400 nm.

On flat pearl sample 2 two force maps were analyzed. The first force map comprised 50 × 50 force curves on a 13.2 μm × 13.2 μm area. The second force map was recorded on a different spot with 50 × 50 force curves on a 21.2 μm × 21.2 μm area. The force scan rate was set to 1 Hz (tip velocity 4.96 μm s$^{-1}$ on first force map, tip velocity 5.01 μm s$^{-1}$ on second force map) and the relative deflection threshold during indentation of the sample was set to 200 nm in both cases.

On flat pearl sample 3 one force map was analyzed. Again 50 × 50 force curves were recorded on a 10.0 μm × 10.0 μm area. The force scan rate was 1 Hz (tip velocity 2.38 μm s$^{-1}$) and the relative deflection threshold during indentation was set to 200 nm.

The deflection sensitivity (the factor that converts the measured voltage on the photo diode into length units during the cantilever deflection) was determined in two different ways for sample 1 and for samples 2 and 3, respectively.

In the case of sample 1 the deflection sensitivity was estimated using the slope of a single deflection–z-piezo position curve.

In the case of samples 2 and 3, deflection curves (map consisting of 10 by 10 deflection curves) were recorded on a cover glass (immersed in liquid) prior to imaging/probing of the flat pearls. The slopes of those deflection–z-piezo position curves were used to estimate the deflection sensitivity.

### 2.3. Image processing and analysis of force maps

All image processing and analysis of the force maps were carried out with the IGOR software package (WaveMetrics, Lake Oswego, OR, USA). For image processing and analysis either the in-built IGOR software or the AFM manufacturer's routines were used. Analysis of the force maps and calculation of mechanical properties of the samples were conducted with home-built IGOR routines.

The Young's modulus of the organic sheets of the flat pearl was determined with the Hertz–Sneddon model (e.g. [17,18] and references given there) corrected for pyramidal indenters (e.g. [19,20]). Here we used the following relation (Eq. (10) in Ref. [20]):

$$F = \frac{1}{\sqrt{2}} \frac{E \tan \alpha}{(1 - \nu^2)} \delta^2 \qquad (1)$$

Eq. (1) relates the force $F$ that is required to indent a sample with Young's modulus $E$ and Poisson ratio $\nu$ to the indentation depth $\delta$. The indenter is described as a pyramidal shaped indenter (pyramid with four regular sides) with a half-opening angle $\alpha$. Here we used a Poisson ratio of $\nu = 0.5$ and a half-opening angle of $\alpha = 18°$, as given by the manufacturer. The spring constant was estimated as described above. Force and indentation were calculated from the recorded deflection and z-piezo position in consideration of the deflection offset and contact point. Then the Young's modulus $E$ was determined from a fit of Eq. (1) to the data. Data were fitted in a specified deflection interval. This lower and upper deflection value corresponds to a force interval where the fit is done. Details of the fit procedure can be found in Ref. [18] and references therein.

## 3. Results and discussion

### 3.1. Topography of flat pearls in aqueous solution

The AFM images of the very early stages (Fig. 2) of overgrown glass slides (flat pearls) show islands of a hard phase – most probable calcite crystals (or spherulitic aragonite crystals) (Fig. 2, white arrows) – in an organic matrix (Fig. 2, black arrow). The left image shows the height signal and the right one shows the remaining deflection signal (error signal). The surface structure of the mineral islands is rough and their diameter ranges from several 100 nm to 100 μm [7]. The morphology can be clearly distinguished from nacreous (polygonal aragonite platelets) material [8]. Growth of aragonite (one of the other calcium carbonate polymorphs) is initiated on top of the large mineral islands. It grows as tablets, with a diameter of 5 to 7 μm in its final form and a height of ∼0.5 μm.

In Fig. 3 an example of two early small stacks of coins (black arrows) on top of a calcite or spherulitic aragonite island (Fig. 3, white arrow) is shown. The left side of the figure shows the height image; the right side the error signal. Prominent features are parallel streaks at the edge of the stacks (Fig. 3, black arrowheads). They stem from the side (flank) of the tip. It touches the crystal because of its high (∼0.5 μm), steep edge, before the very end of the tip can reach the sample [21]. In these regions no valuable data may be extracted. Therefore we did not incorporate the areas with the "parallel streaks" (tip artefacts from scanning the step edges with the flank of the tip and not with the very end of the tip), which can also be seen in Fig. 4B-F, into our data analysis. The tops of the stacks show a flat but slightly corrugated surface. Between two stacks (Fig. 3, white arrowheads) the network of the interlamellar matrix is visible (see also Fig. 4F). The stacks are two or three aragonite platelets in height. Therefore the growth of nacre at this area has just started and the preformed organic matrix contains just a few sheets (see also next section).

The following examples (Fig. 4B–E) show a mature flat pearl, which was incubated between shell and mantle epithelium for more than 5 weeks. Stacks of coins, indicating a rapid growth of nacre, can be found all over the surface. The stacks of coins consist of several aragonite platelets in height. In Fig. 4A an SEM image is shown with a typical distribution of stacks (white arrows pointing on examples) with more than five tablets on top of each other. The inset (Fig. 4A, zoom in) demonstrates that in some cases growth of more than one tablet on top of the underlying one is favoured by the structure of the organic matrix. As it is a network with pores in it, more than one mineral bridge can lead to the formation of the next tablet in the vertical direction (Fig. 4A, inset, white arrowheads) [22].

AFM images of a surface with stacks of coins are shown in Fig. 4B–F. In a profile (along the line in B) the height of the individual tablets (white arrowheads) can be clearly denoted as ∼0.5 μm. In the error signal (Fig. 4C) the tablets are better resolved. In a close-up view in Fig. 4D (height signal) and E (corresponding error signal) the surfaces of the single tablets (white arrowheads) are clearly visible. In between the stacks of coins the interlamellar matrix shows a network-like structure (Fig. 4E, black arrow). Fig. 4F is a close-up view of the interlamellar matrix between the stacks of coins depicted in Fig. 3. This sample was only incubated 3–4 weeks between shell and animal. In this image, it becomes clear that the matrix is located not only between the stacks, but also on top of the uppermost tablet. Long filaments (protein decorated chitin filaments) are resolved (white arrowheads), which run in the interspace of the tablets and also over the tablet itself [6].

This shows that a flat pearl is an ideal instrument to obtain the organic phases of the flat pearls in a condition close to their natural state. The "flat pearl technique" enables the investigation of the

mechanical properties of native, hydrated organic sheets of the interlamellar matrix and other organic phases of flat pearl nacre.

## 3.2. Mechanical properties of flat pearls in aqueous solution

From the recorded deflection and *z*-piezo position data on different areas on the flat pearl samples, the Young's modulus *E* is calculated according to the Hertz–Sneddon model. The applicability of the Hertz–Sneddon model requires several conditions (e.g. Ref. [23], especially Chap. 6). Eq. (1) holds for the indentation of an isotropic and elastic material covering a half-space. The indenter and the indented material contact each other without friction and their dimensions are larger than the contact area.

Considering the SEM image of the organic framework given in Fig. 1B and C we have to state that the sample is not ideal to meet the requirements of the Hertz–Sneddon model. The organic interlamellar matrix consists of several sheets of a fibrous network (see e.g. Figs. 3 and 6 in Ref. [2] or Figs. 6 and 7 in Ref. [5]) and consequently is an anisotropic material. Zaremba et al. [8] described two additional organic phases during the flat pearl growth in *H. rufescens*. First, a "transparent organic sheet" is deposited on the glass support prior to any mineral growth. Second, a "green organic sheet" may be deposited prior to spherulitic mineral growth. The first phase might be similar to the periostracum (see e.g. Sec. 2.3.2. in Ref. [24] for details about the periostracum in molluscs) since a calcite layer is deposited on this phase similar to the outer shell surface. Falini et al. [25] investigated the aforementioned second phase from *H. rufescens* shells in more detail. They note some structural similarity of this phase to the insoluble organic matrix of nacre and compositional similarity to the periostracum. Currently we do not know to what extent these different organic phases behave as an isotropic and linear elastic material.

From the topographic images, we cannot decide whether the organic sheet should be described as a suspended sheet being supported by the stacks of coins, or rather a collapsed stack of several sheets on top of each other. This will depend on the excess area of the sheets and their deformability. From a mechanical point of view, these two situations could be distinguished: a membrane spanning over a pore exhibits a linear force indentation law [26], whereas a collapsed layer of several sheets could, for small indentation, best be described by the Hertz model, which will result in a non-linear force law. Since we have observed the latter, we decided to calculate the Young's modulus for several reasons. First, the Young's modulus as calculated from Eq. (1) is independent of the indenter specifications, in contrast to the slope of the deflection curve. This simplifies comparisons with other materials and measurements. Second, we might expect the Hertz–Sneddon model to be a reasonable approximation if a sufficient number of sheets of the interlamellar matrix lie directly on each other without large liquid-filled compartments or mineral between the sheets.

A hard substrate can influence the apparent Young's modulus of a thin soft layer, as calculated from deflection–*z*-piezo position curves (see e.g. Ref. [27]). Furthermore, we have to account for the possibility that the sheets of the interlamellar organic matrix might not lie on top of each other. Therefore the recorded deflection–*z*-piezo position curves are evaluated in different deflection regimes.

The number of organic sheets of the interlamellar matrix on a flat pearl can only be estimated from the height of the aragonite platelet stacks present on the flat pearl sample close to the spot where the deflection curves are recorded. It is assumed that the crystallization of each aragonite platelet takes place between two preformed sheets (see e.g. Ref. [28] for studies on *H. rufescens*) as well as that these sheets span the area between stacks of mineral platelets. In Ref. [8] the thickness of the "transparent organic sheet" is stated as ∼140 nm. The thickness of the "green organic sheet" is stated to be in the μm range [8,25].

In every case mineral parts are present on the recorded force maps (cf. Figs. 5A and 4F). These areas require a particular consideration. When the indented sample has a stiffness that is comparable to the stiffness of the cantilever the deflection and indentation are of similar magnitude. As the sample becomes stiffer – e.g. on a mineral surface – the slope of the deflection–*z*-piezo position curve approaches 1 in the range where the tip is in contact with the stiff sample and the indentation approaches 0. Fig. 5B shows the slope of the deflection curves in the deflection range of 100 to 150 nm recorded on the area shown in Fig. 5A (Fig. 5 describes the first force map of sample 2). Data points where the slope of the deflection is greater than 0.8 (samples 2 and 3) or 0.9 (sample 1) in a deflection fit range of 100 to 150 nm are excluded from further analysis because at these points a stiff mineral or a thin organic sheet on a stiff mineral is probed. As can be seen by comparison of Fig. 5A and B a slope value greater than 0.8 describes the areas on the force map that consist of a stiff mineral phase or a thin organic sheet on top of a hard phase. In the case of sample 1 we use an increased slope threshold of 0.9 to discriminate between what seems to be mineral and organic phase (see Supplementary information). The necessity of a higher value could be the result of a thin organic layer on a hard substrate or the estimation of the deflection sensitivity from a single force curve.

We proceed by calculating the Young's modulus of every force curve meeting the criteria described in the above paragraph in different deflection regimes. The four regimes, 2–20 nm, 20–40 nm, 40–100 nm and 100–150 nm, are used to cover the major parts of the deflection–*z*-piezo position curves.

Fig. 5C–F shows the resulting values of the logarithm of the Young's modulus (modulus in Pa) as calculated with Eq. (1) in the different fit regimes of sample 2 (first force map). In Fig. 5G the distribution of the Young's modulus is depicted. On this spot two prominent areas can be identified. The one area in the upper right part of the image and force maps shows a strong dependency of the calculated Young's modulus of the deflection fit range whereas the lower left area shows only a moderate dependency of the modulus of the deflection fit range. This behaviour is also clearly visible in the histogram in Fig. 5G. As the deflection fit range is increased to higher deflection values, the "soft" peak on the left side in the histogram moves to higher Young's moduli (peak moves from ∼4.0 to 4.5) and decreases slightly while the peak on the right side in the histogram increases and moves only slightly to higher moduli (peak moves from 5.8 to 5.9; see especially the right flank of the right peak).

If a sample that obeys every prerequisite of the Hertz–Sneddon model is probed and evaluated for the Young's modulus there should be no dependency of the calculated moduli of the deflection fit range.

The AFM deflection image in Fig. 5A gives a first impression of one possible reason for the fit range dependency of the calculated modulus. Some soft areas appear to be fuzzy, indicating that the tip might move the substrate during imaging. This suggests that the top sheet(s) might not be in close contact with underlying sheets.

An exemplary force curve from which the deflection fit range depending Young's moduli can be calculated with the Hertz–Sneddon model is shown in Fig. 6A. In Fig. 6A four force–indentation curves are shown. These four force curves are calculated from one deflection–*z*-piezo position curve from the upper right area of Fig. 5 (*x*-position: 9.35 μm, *y*-position: 12.78 μm; force map point: [35,48] – zero-based counting). Depending on the deflection fit range the fit results in different values of the contact point. This explains the shift of the curves to each other. At least two regimes can be distinguished in these force–indentation curves. Over a large distance of at least 400 nm – we cannot give a precise calculated
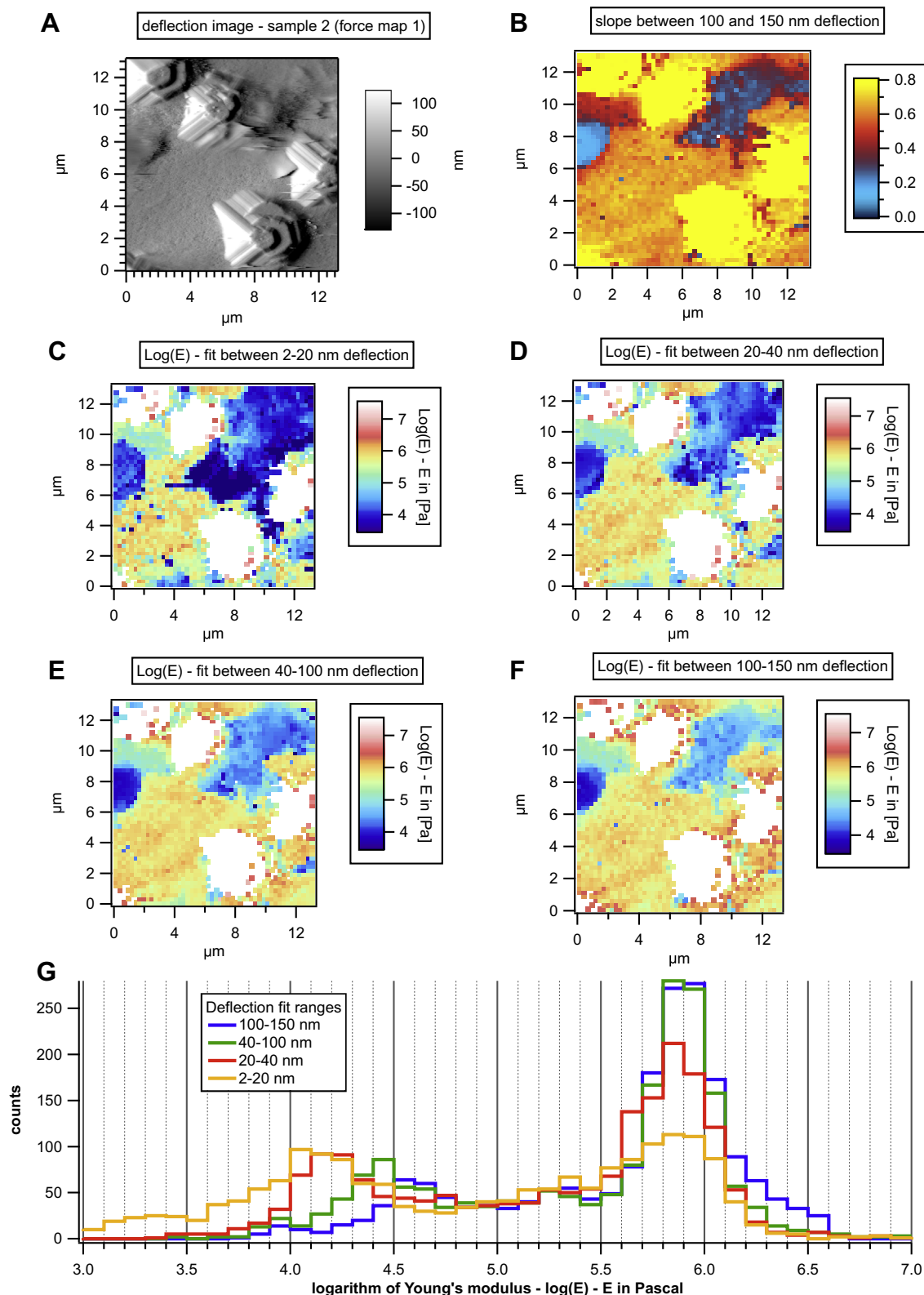
**Fig. 5.** (A) AFM deflection image of the area of sample 2 that is probed by force mapping. (B) Slope of the deflection during approach of the AFM tip to the sample surface as calculated in the deflection range from 100 to 150 nm. (C–F) Logarithm of the Young's modulus calculated from the Hertz–Sneddon model that is fitted to the force–indentation curves in different deflection ranges: 2 to 20 nm (C), 20 to 40 nm (D), 40 to 100 nm (E) and 100 to 150 nm (F). The white areas have not been used for analysis. (G) Distribution of the calculated logarithm of the Young's moduli from the different deflection fit ranges. The binning range is 2 to 8 (shown only 3 to 7) with a bin width of 0.1. The colours indicate the results from different deflection fit ranges: 2–20 nm (ochre), 20–40 nm (red), 40–100 nm (green), 100–150 nm (blue).

indentation depth as the determined contact point from the fit is obviously not reliable if the force–indentation curve shows a strong "non-Hertzian" behaviour – the sample can be indented with a low

force. This is followed by a steeper force–indentation regime. The observed force–indentation relation might be explained by larger spaces between the sheets of the organic matrix – likely filled with
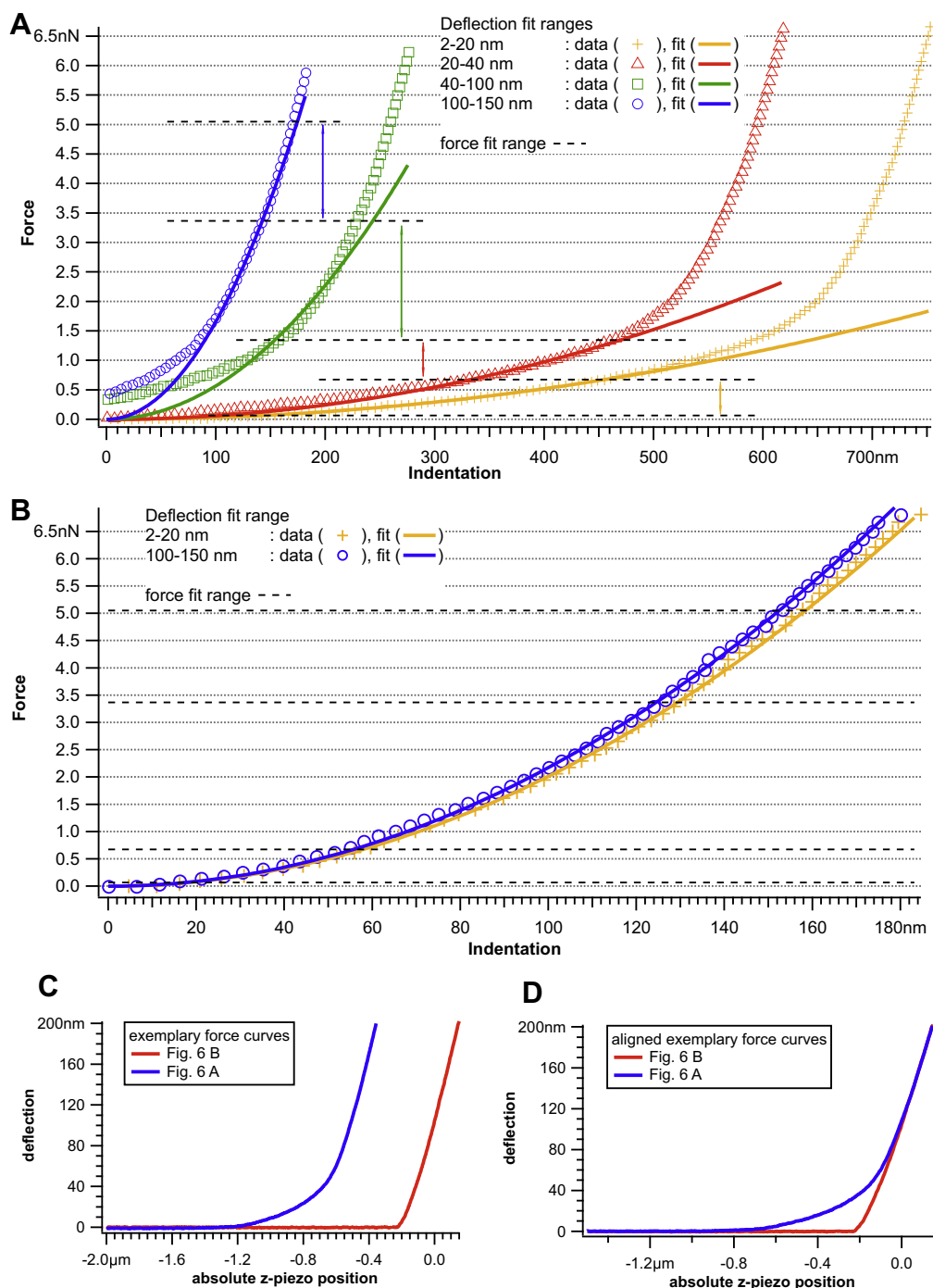
**Fig. 6.** Exemplary force curves from sample 2 shown in Fig. 5. (A) Force–indentation curves (deflection curve from *x*-position: 9.35 μm, *y*-position: 12.78 μm; force map point [35,48] in Fig. 5) in consideration of the contact point as calculated from the Hertz–Sneddon model in different deflection fit ranges. Markers indicate the measured force curves where only every second data point is shown for clarity. The solid lines indicate the fit curve. The different colours describe the different deflection fit ranges: 2–20 nm (ochre/crosses), 20–40 nm (red/triangles), 40–100 nm (green/squares), 100–150 nm (blue/circles). Broken horizontal lines indicate the force fit range. (B) Force–indentation curves (deflection curve from *x*-position: 3.82 μm, *y*-position: 3.56 μm; force map point [14,13] in Fig. 5) in consideration of the contact point as calculated from the Hertz–Sneddon model in different deflection fit ranges. Markers indicate the measured force curves where only every second data point is shown for clarity. The solid lines indicate the fit curve. The different colours describe the different deflection fit ranges: 2–20 nm (ochre/crosses), 100–150 nm (blue/circles). Broken horizontal lines indicate the force fit range. (C) Recorded deflection–*z*-piezo position curves from (A) (blue) and (B) (red). (D) Manually aligned recorded deflection–*z*-piezo position curves from (A) (blue) and (B) (red).

aqueous solution. These spaces could be first reduced with lower forces since the solution should be easily displaced through the porous network and during this initial compression there might be only minor contributions from a deformation of the organic sheet itself.

The exemplary force curve from the lower left area (*x*-position: 3.82 μm, *y*-position: 3.56 μm; force map point: [14,13] – zero-based counting) depicted in Fig. 6B seems to follow the Hertz–Sneddon model quite well. In Fig. 6B the force–indentation curves are shown only for two deflection fit ranges (2–20 nm and

100–150 nm) for clarity. In both cases the fit describes the data well, even outside the fit range. The Young's moduli calculated with the different deflection fit ranges are quite similar: 657 kPa for the 2–20 nm fit range and 710 kPa for the 100–150 nm fit range. These deflection fit ranges correspond to indentations of 16–57 and 125–153 nm, respectively.

In this area we observe neither a strong dependency of the Young's modulus of the deflection fit range (cf. Fig. 5) nor an extended indentation at low forces (cf. Fig. 6A and B). If we compare the deflection–z-piezo position curves (cf. Fig. 6C) of the force curves shown in Fig. 6A and B they differ especially in the lower deflection regime. We aligned them manually to highlight this feature in Fig. 6D.

On sample two, aragonitic stacks of coins can be observed on the areas where the force maps were recorded. The highest stacks of coins observed on sample 2 have at least 3 to 4 aragonite platelets. We cannot state this more precisely since the top height is easily determined but the correct lower reference height is not known. The thickness of one organic sheet is in the order of 20 to 40 nm (see e.g. Fig. 1 in Ref. [29] for a processed cross-sectional nacre specimen of *H. laevigata* or Ref. [28] for studies on *H. rufescens*). If between every aragonite platelet in a stack of coins there is one sheet (as depicted in Fig. 1B for *H. tuberculata*) and they extend over a large area around the stacks of coins we can estimate that on the spot in the lower left area – where the force–indentation curves follow the Hertz–Sneddon model – is at least organic material between 60 and 160 nm thick. Since the deflection–z-piezo position curves have a slope below 0.8 in the deflection range of 100 to 150 nm it is unlikely that the tip is in direct contact with a mineral phase or the glass support of the flat pearls.

Nonetheless, since the structure beneath the imaged surface of the sample is not known we cannot say at which indentation of the sample a buried hard mineral phase or the support influences the measurement.

Force–indentation curves that do not obey the Hertz–Sneddon model over the entire indentation range are observed frequently in every studied sample. On the second force map of sample 2 (see Supplementary information) the two regimes described above and pictured in Fig. 5 can be identified as well. Also on this area – where the force map is recorded – stacks of coins are visible. In contrast to the data presented in Fig. 5 (first force map of sample 2) the "softer" areas cover a larger area of the whole force map compared to Fig. 5. Therefore the peak in the histogram corresponding to the "soft" area is higher (relative to the peak in the histogram corresponding to the "harder" area) on the second force map of sample 2 compared to the first force map of sample 2. But the behaviour found as the deflection fit range is shifted to higher values is the same as in the case described above. The area with a higher Young's modulus increases as the deflection fit range is shifted to higher values. The value of the logarithm of the Young's modulus is slightly increased, from 5.5 to 5.7 (peak position in the histogram). At the same time the "softer" area decreases and the logarithm of the Young's modulus increases slightly from 4.2 to 4.4 (peak position in the histogram).

On both spots on sample 2 where force maps were recorded, "softer areas" can still be identified when the deflection fit range is shifted from 2–20 nm to 100–150 nm for the calculation of the Young's modulus. Also in these areas some force curves that reasonably follow the Hertz–Sneddon model can be found.

The force map on sample 3 (see Supplementary information) is recorded in an area where the hard mineral phase is visible. From the AFM image it can only be deduced that it does not seem to consist of stacks of coins. On sample 3 are only small "soft" areas at the 2 to 20 nm deflection fit range visible. The Young's moduli of these areas increase as the deflection fit range is shifted upwards. Since they do not form a distinct separate peak in the histogram of the

logarithm of the Young's moduli we state the median as well as the 25% and 75% quantiles to describe the fit range dependency of the Young's moduli. For the 2 to 20 nm deflection fit range the range of the logarithm of the Young's modulus is 5.29 to 5.74 (25% quantile to 75% quantile) (median: 5.56). For 20 to 40 nm we have 5.58 to 5.85 (median: 5.72). For 40 to 100 nm we calculate 5.74 to 5.96 (median: 5.84). At the highest deflection fit range the range of the logarithm of the Young's modulus is 5.82 to 6.04 (median: 5.93). Obviously the median increases as the deflection fit range is shifted to higher values. Nevertheless the median is in the same range as in the cases of the analysed force maps of sample 2. On this force map the areas that do not change strongly with the shifted fit range seem to be more scattered across the whole map compared to the situation depicted in Fig. 5.

On sample 3 we found no stacks of coins in the recorded AFM images. Only an unknown hard mineral phase can be imaged. Consequently we can state neither the type of the organic phase nor the thickness of the organic phase present on the sample. For one exemplary force curve that follows the Hertz–Sneddon model the indentations are 16.8 nm to 53.6 nm (deflection fit range 2 to 20 nm; Young's modulus 852.9 kPa) and 117.9 nm to 144.1 nm (deflection fit range 100 to 150 nm; Young's modulus 852.5 kPa).

On sample 1 (cf. Figs. 2, 3, 4F and Supplementary information) we observe the strongest dependency of the Young's modulus of the deflection fit range. The spot where the first force map of sample 1 is taken is similar to that depicted in Fig. 2. The visible hard mineral phase is probably calcite (or spherulitic aragonite). As the deflection fit range is shifted upwards the Young's modulus increases. At the 2–20 nm deflection fit range the range of the logarithm of the Young's modulus is 4.78 to 5.39 (median: 5.14). At the highest deflection fit range the moduli range from 6.69 to 7.04 (median: 6.88). Since we do not know which type of organic is probed we cannot give an estimation of the thickness of the organic phase.

The second and third force maps on sample 1 (see Supplementary information) were recorded subsequently on the area shown in Fig. 4F. The situation is similar to that described in the preceding paragraph. The area does not show "soft" patches at a deflection fit range of 2 to 20 nm; instead, the whole area appears "softer" at the lower deflection fit range compared to the deflection fit range from 100 to 150 nm. During the first probing the range of the logarithm of the Young's modulus is 3.98–4.84 (median: 4.54) at a fit range of 2–20 nm and 6.55–7.02 (median: 6.81) at the highest fit range of 100–150 nm. Interestingly, during the subsequent investigation of the same area the calculated logarithm of the Young's modulus at the lower deflection fit range has shifted to 5.20–5.87 (median: 5.52). The quantiles at the fit range of 100–150 nm are 6.70–7.10 (median: 6.91). The latter values are of similar magnitude as those from the corresponding first measurement on that area. The large difference of the Young's moduli at the 2–20 nm deflection fit range between two subsequent recordings for force curves might be explained by a compression of the sheets on each other during the first probing. That would reduce spaces between the individual sheets so that on the second probing the whole sample appears "harder" at lower indentations.

However, several deflection–z-piezo position curves found on the first and second force map recorded on sample 1 (as well as on the force map of sample 3) allow no proper fit of the Hertz model in the deflection fit range of 2–20 nm, leading to artificial small moduli. In particular, Young's moduli of ~1 kPa are not meaningful. Nevertheless, the large dependency of the Young's modulus of the deflection fit range indicates a "non-Hertzian" sample.

In summary, we have investigated organic phases of flat pearl nacre in their most natural state, which means directly created by the organism with no or minor treatment after the extraction of the flat pearls. Upper estimates of the logarithm of the Young's modulus on the probed samples are 6.91 (8.1 MPa) and 6.88

(7.6 MPa) on sample 1, 5.93 (851 kPa) on sample 3 as well as 6.0 (1 MPa) and 5.7 (501 kPa) on sample 2. As stated above we might overestimate the Young's modulus of sample 1.

The calculated Young's moduli from most of the recorded force curves show a dependency on the deflection fit range. This dependency might be explained by the multilamellar structure of the interlamellar organic matrix and seawater filled spaces between them and/or an influence of a buried hard mineral phase or substrate. Due to the influence of "hard" phases (mineral or glass substrate) the samples might appear "harder" at greater indentations. Since the thickness of the organic phase on buried mineral phases or the glass support is not known we cannot apply the correction of Gavara and Chadwick [30] to the Hertz–Sneddon model. The Hertz–Sneddon model seems to be suitable if sufficient sheets of the interlamellar organic matrix lie directly on top of each other and/or the organic phase has a sufficient thickness.

Nonetheless, on samples 2 and 3 spots with a less pronounced deflection fit range dependency can be found. This is an indication of the partial applicability of the Hertz–Sneddon model and it predicts an upper limit of the Young's modulus near 1 MPa. This is in contrast to the observed values – above 100 MPa – obtained in macroscopic tensile tests [1,5] of the organic layers from demineralized nacre. The higher moduli were obtained by exerting the force parallel – referring to Fig. 5A the force was parallel to the image plane – to the organic layer surface. For AFM investigations the cantilever tip approaches the sample surface from "above" – referring to Fig. 5A the tip approaches the image plane perpendicular. The difference of the obtained Young's moduli with the different experimental approaches might be an expression of the anisotropic nature of the organic layers of nacre. The investigation of the anisotropic mechanical behaviour might contribute to an improved understanding and modelling of the mechanical properties of the nacre as a composite material.

## 4. Outlook

The determination of the mechanical properties of the whole organic matrix as well as of individual sheets of nacre remains challenging. It would be of great interest to reveal the mechanical properties of the organic sheets to elucidate their role in the mechanical properties of the composite structure of nacre.

Furthermore, it is of interest to determine the viscoelasticity of the organic sheets with the AFM (see Ref. [31] as an example for determination of viscoelastic properties of cells). First of all, a frequency-dependent force measurement could provide information about the extent of solution-filled spaces between the sheets or to what extent sheets lie directly on top of each other. Second, the viscoelasticity of the organic phases might provide further insight into the mechanical properties of nacre.

Measurements as described above could be conducted after the treatment of the flat pearl with proteinases. This could provide useful information about whether proteins might be involved in the stability or mechanical properties of the organic framework.

One of the aims is to probe a defined number of compressed sheets or even single organic sheets of the interlamellar matrix. To achieve this we might take advantage of textured or structured supports (i.e. with pits and pillars of defined dimensions, similar to the approach in Ref. [26] for lipid bilayers) for flat pearls instead of cover glass discs. At an early stage of flat pearl growth we might be able to probe non-mineralized organic phases of defined height above a pit. In such a situation the possible effect of the support on the measurements could be reduced or eliminated. Pillars of defined height could be useful for an estimation of the thickness of the probed organic phase.

If the thickness of the organic phase cannot be controlled or determined precisely, we might determine the mechanical properties more precisely if we use tipless cantilevers with small attached spheres and lower indentation ranges.

Finally, it would be of interest to investigate the network-like character (cf. Fig. 4F) of the interlamellar organic sheets. The description of a fibrous network would require information about persistence lengths and the length distribution of the fibrils, the density of cross-links and properties of cross-links (e.g. [32]).

## Appendix A. Supplementary data

*Supplementary Figs. S.1–S.5:* The overall construction of the Supplementary figures is the same as that of Fig. 5. Note that in Figs. S.1–S.3 the colour scale bar of the slope maps has the range 0–0.9 in contrast to Figs. 5, S.4 and S.5. Supplementary data associated with this article can be found, in the online version, at http://dx.doi.org/10.1016/j.actbio.2014.02.050.

## Appendix B. Figures with essential colour discrimination

Certain figures in this article, particularly Figs. 1, 5, and 6 are difficult to interpret in black and white. The full colour images can be found in the on-line version, at http://dx.doi.org/10.1016/j.actbio.2014.02.050).

## References

[1] Dastjerdi AK, Rabiei R, Barthelat F. The weak interfaces within tough natural composites: experiments on three types of nacre. J Mech Behav Biomed Mater 2012;19:50–60.

[2] Heinemann F, Launspach M, Gries K, Fritz M. Gastropod nacre: structure, properties and growth – biological, chemical and physical basics. Biophys Chem 2011;153:126–53.

[3] Sun J, Bhushan B. Hierachical structure and mechanical properties of nacre: a review. RSC Adv 2012;2:7617–32.

[4] Chen P-Y, McKittrick J, Meyers MA. Biological materials: functional adaptions and bioinspired designs. Prog Mater Sci 2012;57:1492–704.

[5] Bezares J, Asaro RJ, Hawley M. Macromolecular structure of the organic framework of nacre in Haliotis rufescens: implications for mechanical response. J Struct Biol 2010;170:484–500.

[6] Launspach M, Rückmann K, Gummich M, Rademaker H, Doschke H, Radmacher M, et al. Immobilisation and characterisation of the demineralised, fully hydrated organic matrix of nacre—an atomic force microscopy study. Micron 2012;43:1351–63.

[7] Fritz M, Belcher AM, Radmacher M, Walters DA, Hansma PK, Stucky GD, et al. Flat pearls from biofabrication of organized composites on inorganic substrates. Nature 1994;371:49–51.

[8] Zaremba CM, Belcher AM, Fritz M, Li Y, Mann S, Hansma PK, et al. Critical transitions in the biofabrication of abalone shells and flat pearls. Chem Mater 1996;8:679–90.

[9] Su X, Belcher AM, Zaremba CM, Morse DE, Stucky GD, Heuer AH. Structural and microstructural characterization of the growth lines and prismatic microarchitecture in red abalone shell and the microstructures of abalone "flat pearls". Chem Mater 2002;14:3106–17.

[10] Lin AY-M, Chen P-Y, Meyers MA. The growth of nacre in the abalone shell. Acta Biomater 2008;4:131–8.

[11] Fleury C, Marin F, Marie B, Luquet G, Thomas J, Josse C, et al. Shell repair process in the green ormer Haliotis tuberculata: a histological and microstructural study. Tissue Cell 2008;40:207–18.

[12] Gries K, Kröger R, Kübel C, Schowalter M, Fritz M, Rosenauer A. Correlation of the orientation of stacked aragonite platelets in nacre and their connection via mineral bridges. Ultramicroscopy 2009;109:230–6.

[13] Weiss IM, Renner C, Strigl MG, Fritz M. A simple and reliable method for the determination and localization of chitin in abalone nacre. Chem Mater 2002;14:3252–9.

[14] Butt H-J, Jaschke M. Calculation of thermal noise in atomic force microscopy. Nanotechnology 1995;6:1–7.

[15] Hutter JL, Bechhoefer J. Calibration of atomic-force microscope tips. Rev Sci Instrum 1993;64:1868–73.

[16] Cleveland JP, Manne S, Bocek D, Hansma PK. A nondestructive method for determining the spring constant of cantilevers for scanning force microscopy. Rev Sci Instrum 1993;64:403–5.

[17] Sneddon IN. The relation between load and penetration in the axisymmetric Boussinesq problem for a punch of arbitrary profile. Int J Eng Sci 1965;3:47–57.

[18] Radmacher M. Measuring the elastic properties of living cells by the atomic force microscope. In: Jena BP, Hörber HJK, editors. Methods in cell biology. San Diego, CA: Academic Press; 2002. p. 67–90.

[19] Bilodeau GG. Regular pyramid punch problem. J Appl Mech 1992;59:519–23.

[20] Rico F, Roca-Cusachs P, Gavara N, Farré R, Rotger M, Navajas D. Probing mechanical properties of living cells by atomic force microscopy with blunted pyramidal cantilever tips. Phys Rev E 2005;72:1–10.

[21] Kacher CM, Weiss IM, Stewart RJ, Schmidt CF, Hansma PK, Radmacher M, et al. Imaging microtubules and kinesin decorated microtubules using tapping mode atomic force microscopy in fluids. Eur Biophys J 2000;28:611–20.

[22] Schaeffer TE, Ionescu-Zanetti C, Proksch R, Fritz M, Walters DA, Almqvist N, et al. Does abalone nacre form by heteroepitaxial nucleation or by growth through mineral bridges? Chem Mater 1997;9:1731–40.

[23] Fischer-Cripps AC. Introduction to contact mechanics. 2nd ed. New York: Springer; 2007.

[24] de Paula SM, Silveira M. Studies on molluscan shells: contributions from microscopic and analytical methods. Micron 2009;40:669–90.

[25] Falini G, Sartor G, Fabbri D, Vergni P, Fermani S, Belcher AM, et al. The interstitial crystal-nucleating sheet in molluscan *Haliotis rufescens* shell: a biopolymeric composite. J Struct Biol 2011;173:128–37.

[26] Mey I, Stephan M, Schmitt EK, Müller MM, Ben Amar M, Steinem C, et al. Local membrane mechanics of pore-spanning bilayers. J Am Chem Soc 2009;131:7031–9.

[27] Domke J, Radmacher M. Measuring the elastic properties of thin polymer films with the atomic force microscope. Langmuir 1998;14:3320–5.

[28] Nakahara H, Bevelander G, Kakei M. Electron microscopic and amino acid studies on the outer and inner shell layers of *Haliotis rufescens*. Venus 1982;41:33–46.

[29] Gries K, Kröger R, Kübel C, Fritz M, Rosenauer A. Investigations of voids in the aragonite platelets of nacre. Acta Biomater 2009;5:3038–44.

[30] Gavara N, Chadwick RS. Determination of the elastic moduli of thin samples and adherent cells using conical atomic force microscope tips. Nat Nanotechnol 2012;7:733–6.

[31] Alcaraz J, Buscemi L, Grabulosa M, Trepat X, Fabry B, Farré R, et al. Microrheology of human lung epithelial cells measured by atomic force microscopy. Biophys J 2003;84:2071–9.

[32] Wilhelm J, Frey E. Elasticity of stiff polymer networks. Phys Rev Lett 2003;91:108103.